Journal of CO_2 Utilization xxx (2015) xxx–xxx

Contents lists available at ScienceDirect

Journal of CO_2 Utilization

journal homepage: www.elsevier.com/locate/jcou

Hierarchical TiO_2 nanofibres as photocatalyst for CO_2 reduction: Influence of morphology and phase composition on catalytic activity

Patricia Reñones[a], Alicia Moya[b], Fernando Fresno[a], Laura Collado[a], Juan J. Vilatela[b,*], Víctor A. de la Peña O'Shea[a,*]

[a] Photoactivated Processes Unit, IMDEA Energy Institute, Parque Tecnológico de Móstoles, Avda. Ramón de la Sagra 3, 28935 Móstoles, Madrid, Spain
[b] IMDEA Materials Institute, Eric Kandel 2, 28906 Getafe, Madrid, Spain

ARTICLE INFO

Article history:
Received 31 October 2015
Received in revised form 1 April 2016
Accepted 2 April 2016
Available online xxx

Keywords:
CO_2 photoreduction
Artificial photosynthesis
Hierarchical TiO_2 fibres
Electrospinning
Sol-gel

ABSTRACT

In this research work, the gas phase CO_2 photocatalytic reduction using water as electron donor has been performed using hierarchical assemblies of mesoporous TiO_2 1-D nanofibres synthesised by a combination of electrospinning and sol–gel methods. In order to compare the effect of the crystallisation step on oxygen vacancies and conductivity, two different annealing conditions have been undertaken: under a high Ar flow ("TiO_2 Fibres-A" sample) and under static Ar ("TiO_2 Fibres B" sample). Moreover, these materials have been compared with individualised TiO_2 nanoparticles prepared by a sol-gel procedure. CO and H_2 are detected as major products with all photocatalysts, with lower amounts of CH_4 and CH_3OH. The TiO_2 nanofibres exhibit better results than the sol-gel photocatalyst, behaviour that may be ascribed to an improved nanocrystals connection, which favours a fast charge transport along the grain boundaries, as measured by electrochemical impedance spectroscopy (EIS). The highest CO_2 reduction activity is achieved with the TiO_2 Fibres B catalyst, which gives rise to ca. 4 and 2.5 times higher H_2 and CO production, respectively, than the TiO_2 Fibres-A one. This sample is composed of a mixture of anatase and rutile crystalline phases (80:20), leading to a decrease in the electron-hole recombination rate observed by photoluminescence (PL) measurements.

1. Introduction

A promising strategy for CO_2 valorisation is photocatalytic reduction to produce fuels and value-added chemicals, using water as reducing agent. This process, also called Artificial Photosynthesis (AP), is mainly based on the use of semiconductor catalysts, and is particularly advantageous considering that reactions can be driven under mild conditions and using a sustainable energy source [1]. However, although intensive efforts have been devoted in the last years to improve photocatalytic efficiencies for carbon dioxide reduction, the literature still reports very low quantum yields, especially when water is used as the only electron donor without any sacrificial reagent [2]. Regarding photocatalytic systems, TiO_2 is one of the most studied materials in this field [3], because of its strong photocatalytic performance, easy availability, long-term stability, nontoxicity and low cost. However, the performance of TiO_2 depends strongly on its crystalline phase, dimensions and morphology, since these parameters exert a crucial influence on the chemical and physical properties of this semiconductor [4,5]. For instance, TiO_2 nanocrystals tend to aggregate into larger particles, resulting in reduced surface area and higher charge recombination rates [6,7]. In last years, in order to improve the overall photocatalytic performance, different synthetic strategies or modifications have been developed, including band structure engineering, metal and non-metal doping and deposition of metal nanoparticles (NPs), with the aim of modifying the textural, structural and optoelectronic properties [8–10].

Among these approaches, several authors have demonstrated than the combination of 1D morphologies (i.e. rods, tubes, fibres) and mesoporous properties would provide titania with unique properties and multiple functions, favouring the electron-hole separation and increasing the electron diffusion coefficient [9,11–14]. Furthermore, the porous structure has been considered as an effective way to improve the light adsorption capacity because of increased surface area and multiple interparticle scattering, leading to the enhancement of photocatalytic reaction rates due to improved light harvesting abilities and intrinsic photocatalytic performance [8,15,16].

* Corresponding authors.
E-mail addresses: juanjose.vilatela@imdea.org (J.J. Vilatela), victor.delapenya@imdea.org (V.A. de la Peña O'Shea).

http://dx.doi.org/10.1016/j.jcou.2016.04.002
2212-9820/

Nowadays, a great number of methods has been developed to prepare nanostructured TiO_2, including sol–gel, hydrothermal synthesis, electrospinning, or combinations of them. In particular, electrospinning of TiO_2 nanofibres has been demonstrated to be a simple, high yield, low-cost, and effective strategy to prepare ultrafine 1D-TiO_2 even at a large scale [17–21]. Electrospinning involves the application of a high voltage to a viscous precursor gel which then traverses some distance to an oppositely charged conductive surface. As the resulting jet travels towards the grounded target, fibres form and deposit on the substrate of choice [17,22]. Several authors have shown that electrospun TiO_2 fibres show an enhanced photocatalytic activity due to the characteristic intimately stacked porous structure, which improve the optoelectronic properties facilitating light absorption on the surface and its transmission, increasing the charge separation through interparticle charge transfer along the TiO_2 fibre [17,23,24].

The present work focuses on the study of the effect of the morphology and the structure of electrospun TiO_2 nanofibres on their activity for gas-phase CO_2 photoreduction using water as electron donor. The activity and the selectivity of these nanofibres are compared with those of TiO_2 nanoparticles prepared by the sol-gel method. The experiments were performed using UV light and higher photocatalytic activities were observed for the fibres prepared by annealing in static Ar, mainly due to a combination of the morphological properties of the fibre and to the presence of anatase and rutile phase, which leads to a synergy effect decreasing the e—h+ recombination rate compared to the sol-gel-obtained TiO_2 nanoparticles.

2. Experimental

2.1. Preparation of catalysts

All chemicals were purchased with analytical grade from Sigma-Aldrich and used without further purification. TiO_2 nanofibres were synthesised by a combination of the sol-gel method and the electrospinning technique. A 10 wt.% of polyvinyl pyrrolidone (PVP) solution in ethanol was stirred and then mixed with the inorganic precursor solution (63.5 wt.% of titanium tetraethoxide in ethanol and a few drops of acetic acid). The solution was vigorously stirred to obtain a uniform dispersion. Then, the solution was placed in a syringe and fed into an electrospinning set-up (Nanon 01A, MECC CO., LTD.). Fibres were collected on an aluminium foil using an applied voltage of 18 kV, a flow rate of 0.7 mL/h and a distance between the tip and the collector of 15 cm. After electrospinning, the samples were annealed in air at 400 °C for 150 min to remove the polymer. After that, crystallisation of titania was performed at 500 °C for 1 h under inert atmosphere, which was previously found to help in the photocatalytic properties of the material [17]. In this study we used different Ar atmospheres: under a high Ar flow for "TiO_2 Fibres-A" sample and under static Ar for "TiO_2 Fibres B" sample.

TiO_2 nanoparticles were also prepared by a standard sol-gel route for comparison with the nanofibre structure produced by electrospinning. In a typical route, 3 mL of titanium tetraethoxide was dissolved in 10 mL of absolute ethanol and hydrolysed with a few drops of acetic acid. The mixture was vigorously stirred at 80 °C for 24 h. A yellowish powder was obtained which was annealed at 500 °C for 1 h in static Ar atmosphere. This sample was named "TiO_2 Sol-gel".

2.2. Catalyst characterisation

Morphological analysis of the fibres was carried out using a scanning electron microscope at 4–10 keV (SEM, EVO MA15, Zeiss Model) and a high resolution transmission electron microscope (HRTEM, JEOL JEM 3000F) operating at 300 kV. Phase analysis was performed using X-Ray Diffraction (XRD) with a X'Pert MD Analytical diffractometer, using Cu Kα radiation. From XRD patterns, average crystal sizes were calculated using Scherrer's formula [25] and the anatase/rutile mass ratio were estimated according to Spurr's equation [26]. Raman spectroscopy was performed with a Jasco NRS-5100 spectrometer using a laser of 532 nm of wavelength at 5.3 mW power. Nitrogen adsorption-desorption isotherms were carried out on a Micrometrics ASAP 2010 apparatus at 77 K. Specific surface areas (according to BET) and porosities (according to BJH) were determined assuming 0.162 nm^2 as the N_2 molecule area. Ultraviolet-visible diffuse reflectance spectra (UV-vis DRS) were obtained in a Lambda 1050 Perkin Elmer equipment in the range of 250–800 nm, using $BaSO_4$ as a blank reference. Fluorescence spectra of solid samples were measured in a Fluorescence Spectrometer Perkin Elmer LS 55, using 300 nm as excitation wavelength and a cut-off filter at 350 nm.

Electrochemical impedance spectroscopy (EIS) studies were carried out in a three-electrode cell using a potentiostat (Bio-Logic SP-200) with AC signal of 10 mV amplitude in the frequency range of 10 kHz–10 mHz with an applied bias of −0.6 V. Pt was used as counter electrode and a Ag/AgCl electrode was used as reference electrode, while the working electrode was prepared by deposition of the TiO_2 sample onto a Ti plate substrate. The powdered sample (1 mg) was ultrasonicated in 1 mL of ethanol to disperse it. The slurry was then spread onto the Ti plate (area of 2 cm^2) at dried at 90 °C for 1 h. Aqueous 0.1 M Na_2SO_4 was used as electrolyte with pH adjusted at 2 with H_2SO_4.

2.3. CO_2 photoreduction tests

CO_2 photoreduction experiments were conducted in continuous flow mode in a gas-phase stainless steel photoreactor, with an effective volume of 190 mL and provided with a borosilicate window for irradiation. The powdered catalysts (0.1 g) were

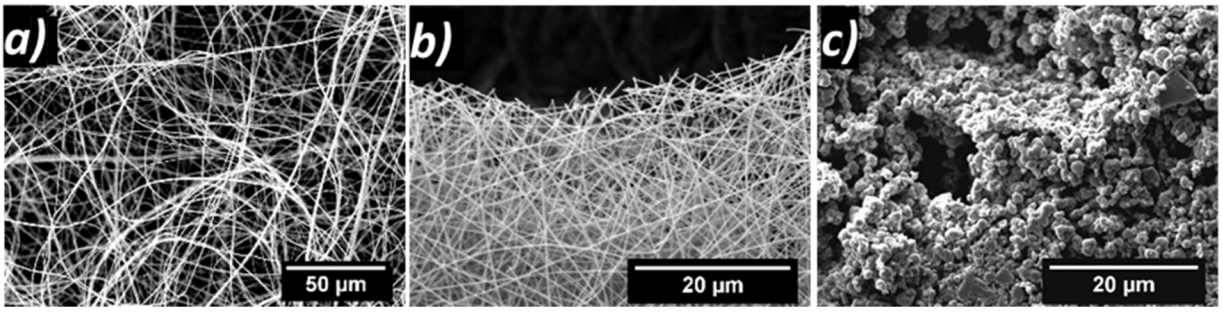

Fig. 1. SEM images of catalysts: (a) fibres before calcination, (b) fibres after calcination and (c) TiO_2 Sol-gel.

Please cite this article in press as: P. Reñones, et al., Hierarchical TiO_2 nanofibres as photocatalyst for CO_2 reduction: Influence of morphology and phase composition on catalytic activity, J. CO_2 Util. (2016), http://dx.doi.org/10.1016/j.jcou.2016.04.002

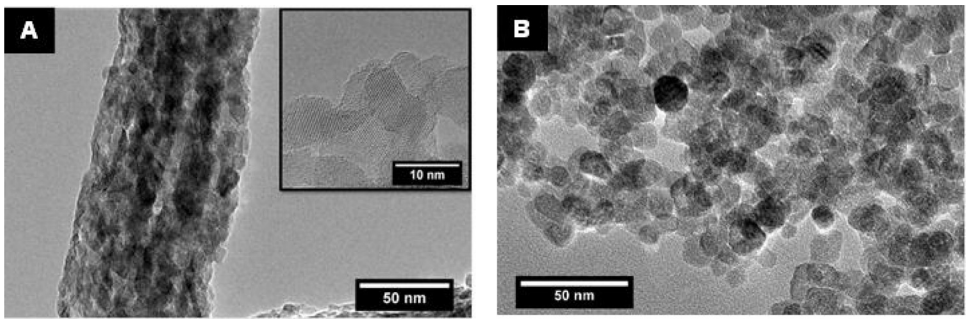

Fig. 2. TEM images: (A) TiO_2 Fibres; (B) TiO_2 Sol-gel.

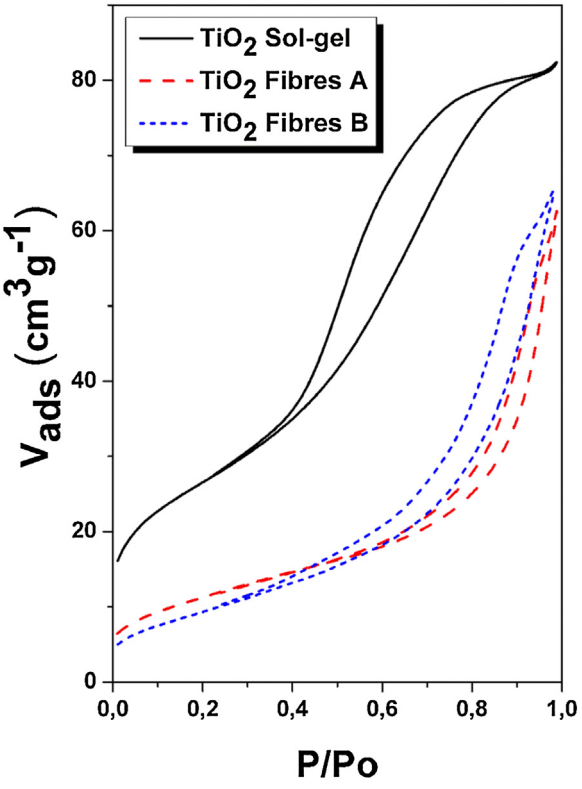

Fig. 3. Nitrogen adsorption-desorption isotherms of all catalysts.

deposited on a glass microfibre filter from aqueous suspensions. Pure carbon dioxide (99.9999%, Praxair) and water (Milli-Q) were fed into the reaction system with a CO_2:H_2O molar ratio of 7.25 by means of a Controlled Evaporator Mixer (CEM). The reaction conditions were set at 2 bar and 50 °C. The photocatalytic measurements were performed using four UV lamps of 6W (λ_{max} = 365 nm). In-line analyses of the reactor outlet gas were performed every 22 min. using a Bruker 450 gas chromatograph equipped with three columns (BR-Q Plot, BR-Molsieve 5A and CP-Sil 5B), three detectors (2 FID and 1 TCD) and a methanizer.

The reactor was firstly degassed at 50 °C under vacuum and then purged with Ar (100 mL/min) for 1 h in order to remove any residual compounds weakly adsorbed on the surface of the catalyst. Then a CO_2 and H_2O mixture was fed in the dark for 1 h in order to establish an adsorption-desorption balance at the reaction temperature. Prior to illumination, the reactor was pressurized and kept at the reaction flow rate for another 1 h. All photocatalytic tests were investigated over a period of 20 h of irradiation.

Apparent Quantum Yields (AQY) were calculated according to Eq. (1), considering the number of electrons required to obtain each product, and measuring the incident spectral irradiance on the surface of the catalyst below 400 nm by means of an optical fibre StellarNet UVNb-50 spectrometer.

$$AQY(\%) = \frac{reacted\ electrons}{incident\ photons} \times 100 \quad (1)$$

3. Results and discussion

3.1. Characterisation of TiO_2 photocatalysts

The morphological properties of the prepared materials were studied by electron scanning microscopy. The as-electrospun samples consist of fibres of several microns length and diameters of ca. 800 nm (Fig. 1) composed by a mixture of TiO_2 nanoparticles embedded in the polymer, with typically around 50 wt.% of each component [17]. The removal of the polymer by calcination results in a reduction in the length of the fibres and, especially, in a decrease of fibre diameter from about a micron to a few hundred nanometres, as shown in the SEM images in Fig. 1(a,b). On the other hand, TiO_2 produced by a standard sol-gel process and annealed in the same conditions forms aggregates of nanoparticles as shown in Fig. 1(c).

The aggregation state of TiO_2 crystals in both configurations (fibres and nanoparticles) can be observed in the TEM images displayed in Fig. 2A, which shows a fibre formed by nanoparticles of TiO_2 that are connected between them presenting large interfaces similar to grain boundaries (see inset). In contrast,

Table 1
Structural, textural and electronic properties of the synthesised photocatalysts.

	Crystalline phases	Anatase crystal size (nm)	Rutile crystal size (nm)	S_{BET} ($m^2\,g^{-1}$)	Pore size (nm)	E_g (eV)
TiO_2 Sol-gel	Anatase	17	–	95.5	4.7	3.2
TiO_2 Fibres A	Anatase (93%) Rutile (7%)	15	21	35.4	20.0	3.1
TiO_2 Fibres B	Anatase (81%) Rutile (19%)	17	16	41.4	10.8	3.1

Please cite this article in press as: P. Reñones, et al., Hierarchical TiO_2 nanofibres as photocatalyst for CO_2 reduction: Influence of morphology and phase composition on catalytic activity, J. CO_2 Util. (2016), http://dx.doi.org/10.1016/j.jcou.2016.04.002

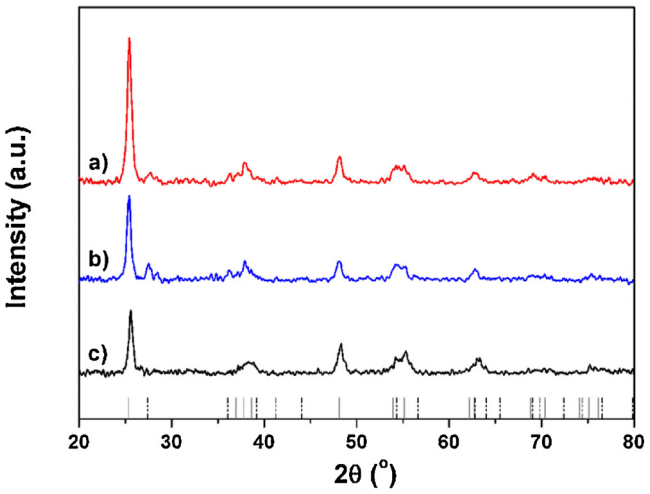

Fig. 4. XRD patterns of (a) TiO_2 Fibres A, (b) TiO_2 Fibres B, and (c) TiO_2 Sol-gel. Anatase pattern (solid vertical lines) corresponds to ICDD Powder Diffraction File (PDF) # 01-083-2243, while that of rutile (dashed vertical lines) to PDF # 01-078-2485.

TiO_2 Sol-gel (Fig. 2B) consists of agglomerations of randomly distributed nanoparticles.

The effect of the morphology on the textural properties of all samples was studied by N_2 adsorption/desorption isotherms (Fig. 3), with the obtained results in terms of BET surface area and pore size summarised in Table 1. A decrease in the surface area is observed in the case of the fibre materials respect to TiO_2 Sol-gel. Considering that both types of catalysts are formed by crystals of similar size, the decrease in the surface area further supports that a structure of interconnected nanocrystals is formed in TiO_2 fibre samples, as shown in Figs. 1 and 2. Regarding pore sizes, all catalysts show values in the mesopore range which are ascribed to interparticle voids. However, the fibres samples exhibit higher values in the pore size, with those annealed under Ar flow (TiO_2 Fibres-A) presenting higher-sized pores as well as a slightly lower surface area.

Structural analysis of the catalysts by XRD shows the characteristic diffraction peaks of the anatase phase in all cases, as shown in Fig. 4. However, both samples of TiO_2 fibres also present diffraction peaks of the rutile phase, indicating that TiO_2 fibre configuration promotes a phase transformation that occurs at higher temperatures for powder samples [17]. This is ascribed to the effect of one-dimensional confinement in the electrospun fibres on the crystallisation of TiO_2 nanocrystals. In this kind of structures, the large interface between anatase nanoparticles favours the nucleation kinetics of rutile nanocrystals [27].

Average crystal sizes calculated using the Scherrer equation are collected in Table 1. All the samples present anatase nanocrystals of around 15 nm diameter indicating that crystal size has not been significantly affected by the morphology of the sample, neither by using different Ar atmospheres (static or dynamic) during the annealing. The anatase and rutile mass contents estimated from Spurr's equation [26] are also collected in Table 1, where a higher amount of rutile in the fibres annealed in static argon is observed.

From TEM images it was possible to differentiate between the crystals corresponding to anatase and rutile phases by calculating the interplanar distances, as shown in Fig. 5, where examples of analysed TEM images are displayed. These results point in the same direction, although at a local scale, as those obtained from XRD, with the TiO_2 Sol-gel catalyst containing only the anatase phase and the TiO_2 fibres samples containing both phases in all the studied areas. In addition, the diameter of the TiO_2 fibres (insets in Fig. 5) change from one type to the other, averaging ca. 105 nm for TiO_2 Fibres-A and 125 nm for TiO_2 Fibres B.

Further structural characterisation was completed using Raman spectroscopy (Fig. 6). All the samples show the active modes of TiO_2 anatase, with only shoulders at the high energy size of the

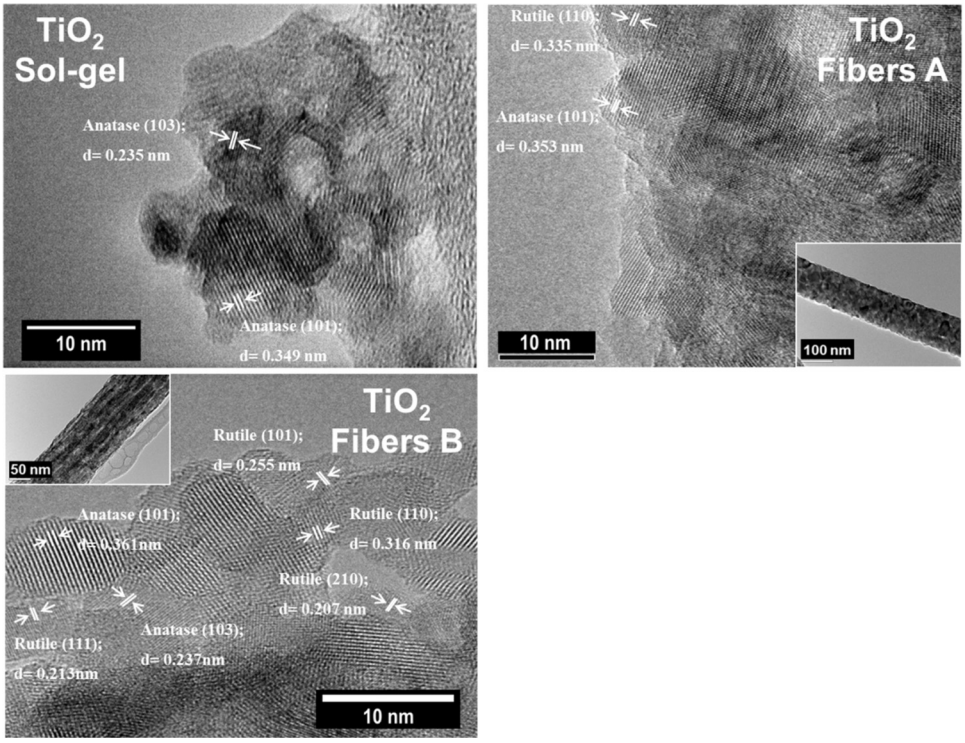

Fig. 5. HRTEM images of prepared catalysts. Interplanar distances of selected crystalline domains are indicated. The insets show lower magnification images of the fibre samples.

Please cite this article in press as: P. Reñones, et al., Hierarchical TiO_2 nanofibres as photocatalyst for CO_2 reduction: Influence of morphology and phase composition on catalytic activity, J. CO_2 Util. (2016), http://dx.doi.org/10.1016/j.jcou.2016.04.002

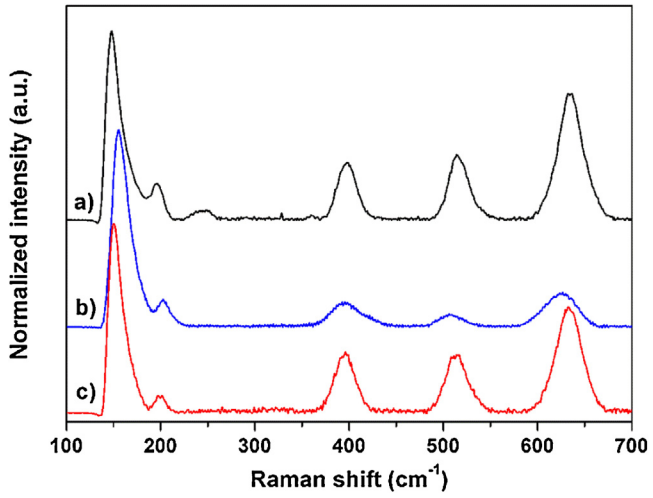

Fig. 6. Raman spectra of (a) Sol-gel, (b) Fibres A and (c) Fibres B TiO_2 catalysts.

band at ca. 400 cm^{-1} and the low energy side of the band at ca. 625 cm^{-1} assignable to rutile in Fibres B sample [28]. This should be due to the fact that Raman spectroscopy is a surface sensitive technique and, especially, that the volume of analysed material is significantly lower than in XRD. In the same line, the broad band observed in the TiO_2 Sol-gel spectrum can be attributed to small amounts of rutile or brookite not observed in X-ray diffractograms [29,30]. The observed peaks assigned to anatase phase correspond to the vibrational modes at 143 (E_g), 196 (E_g), 396 (A_{1g}), 516 (A_{1g} or B_{1g}) and 639 (E_g) cm^{-1} in the bulk [28]. However, the present samples display a blue shift in comparison with the vibrations reported for the bulk material which is usually assigned to phonon confinement in small crystals [31]. However, in this case, each sample presents a different shift even when the crystal size calculated by XRD is quite similar (Table 1). As it was previously mentioned, the use of electrospinning technique in combination with sol-gel produces a structure of interconnected nanocrystals that are in close contact forming interfaces as grain boundaries. The interface plays an important role in the structure of the TiO_2 fibres. On the one hand, the TiO_2/TiO_2 interfaces facilitate the nucleation of rutile crystals which produces a slight disorder in the fibre structure that explain the higher Raman shift observed in the electrospun fibres in comparison with the nanoparticles. On the other hand, the TiO_2/TiO_2 interfaces produce more defects by sharing oxygen at the interface. Therefore, the blue shift of the electrospun samples is attributed to oxygen vacancies that are more pronounced in the case of the Fibres-A sample which was annealed under higher Ar flow. As is well known, Ar atmosphere could partially reduce TiO_2, creating more oxygen vacancies [32].

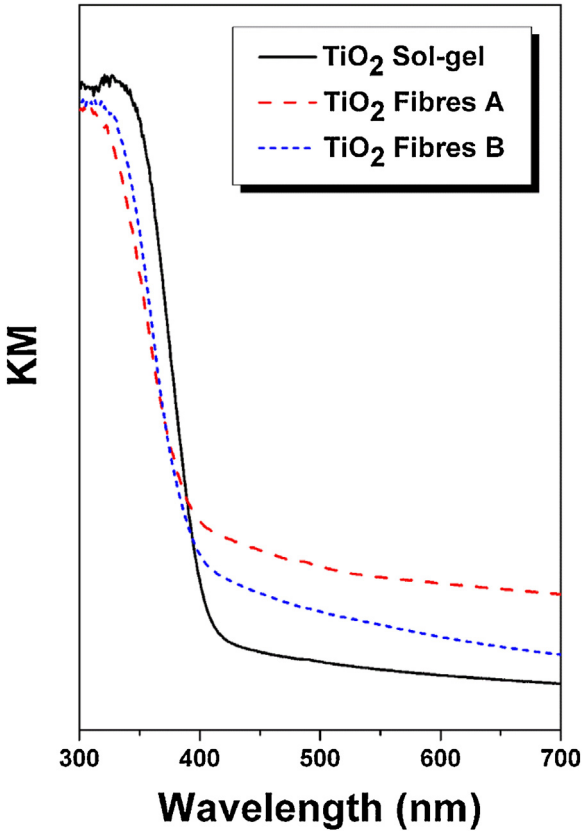

Fig. 7. Diffuse reflectance UV-Vis spectra of synthesised catalysts.

The electronic properties of the obtained catalysts were studied by means of UV-vis and photoluminescence spectroscopies. Fig. 7 shows UV-vis absorption spectra. All the samples show an onset around 400 nm corresponding to the excitation of electrons from the valence band to the conduction band of TiO_2. The sharp absorption onset indicates that these samples have little amorphous content. The higher absorption in the visible region observed in the TiO_2 Fibres catalysts may be due to surface states or defects producing in-gap levels located near the band edge (Urbach tail), which can be related to oxygen vacancies [33], in line with the observations made from Raman spectra.

Band gap energies were calculated from UV-vis spectra using $(\alpha h\nu)^{1/2}$ vs. $h\nu$ plots as corresponds to indirect band-to-band transitions in TiO_2 [34] (Table 1), with results in good agreement with previously reported values [35]. TiO_2 Sol-gel, where only the anatase phase is observed, exhibits a slightly higher band gap (Eg = 3.2 eV) in comparison with the TiO_2 Fibres A and B (E_g = 3.1 eV). These change can be attributed to the presence of rutile (E_g = 3.0 eV, [35]) nanoparticles in the fibre materials.

Fig. 8 depicts the photoluminescence (PL) spectra of all catalysts in the wavelength range of 300–800 nm. A broad band from 350 to 600 nm composed by multiple emission contributions is observed for all samples. The first peaks located at the beginning of the band (below 400 nm) can be assigned to the contribution of recombination process (conduction band → valence band), in this case not totally observed due to the used emission cut-off filter at 350 nm. PL bands appearing in the visible region (400–600 nm) are mostly associated with excitons, which mainly result from surface oxygen vacancies and defects. In general terms, weaker emission signal implies a lower recombination rate of photogenerated electron–hole pairs [36]. Therefore, from the spectra shown in Fig. 8, a recombination rate in the order TiO_2 Fibres A > TiO_2 Sol-Gel > TiO_2 Fibres B can be deduced.

In order to understand the influence of the network of nanoparticles as an improved system for charge transfer and transport, EIS measurements were performed in the dark at −0.6 V applied potential, because the charge accumulation and the charge transfer processes that occur at the TiO_2/electrolyte interface are more predominant at this voltage. Fig. 9 shows the Nyquist plot of the catalysts under dark conditions. Two semicircles are observed; the one at higher frequencies is partially depressed (see top left inset) and corresponds to the substrate/electrolyte interface. The semicircle at low frequencies (right part of the Nyquist plot) is determined by the processes between the TiO_2 and the electrolyte interface. The smallest semicircle reveals the lowest charge transfer resistance, higher conductivity of the TiO_2 fibres samples which means a higher efficiency in the charge transfer process.

EIS spectra were analysed using a transmission model (right bottom inset in Fig. 9) that has been previously applied for

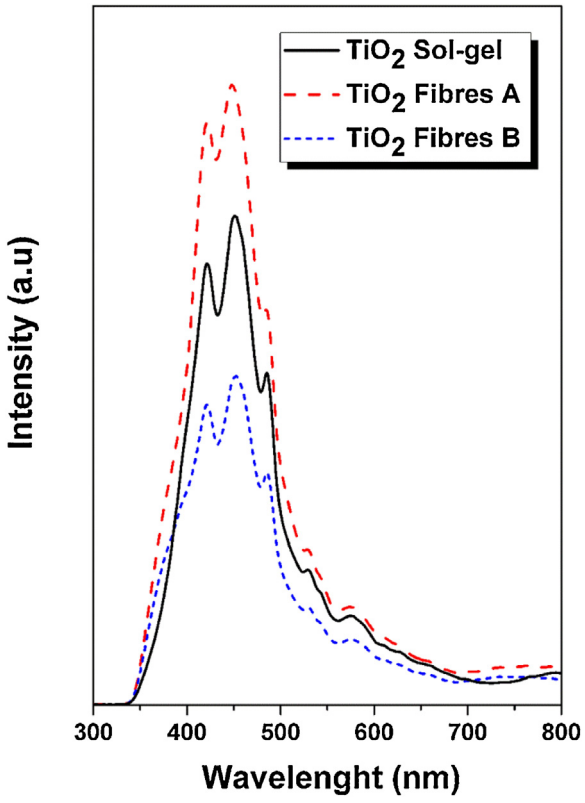

Fig. 8. Photoluminescence spectra of fibre and sol-gel catalysts.

nanocrystalline porous TiO_2 systems of similar configurations [37]. The model consists in a series resistance (R1), a capacitance from substrate/electrolyte interface (Q1), a transport resistance in TiO_2 (R2) and a charge transfer resistance (R3) at the TiO_2/electrolyte interface in parallel with a capacitance of the charge storage in TiO_2 electrode (Q3). Constant phase elements (Q) instead of pure capacitors (C) were employed as they describe better the non-ideal response of the electrodes. Thus, the impedance of a constant phase element is $Z_Q = 1/C_0(j\omega)^a$ where the exponential *a* indicates how close it is to the capacitor behaviour (in which case a = 1). The EIS Nyquist curves reveal that an increase in the interfacial contact between nanoparticles in the fibre structure favours the transport

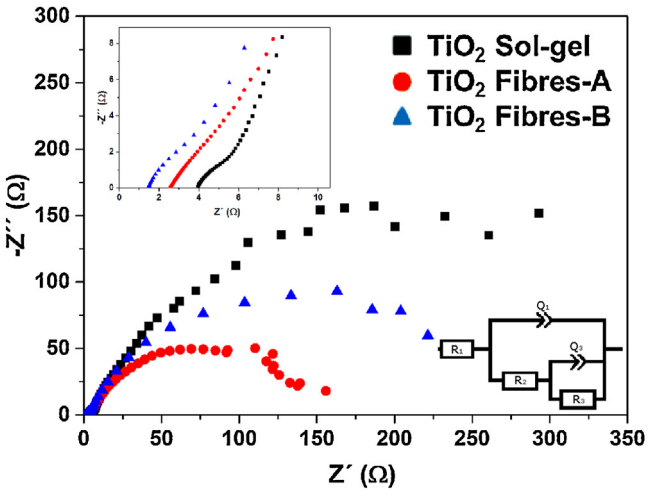

Fig. 9. EIS Nyquist plots of TiO_2 catalysts at an applied voltage of −0.6 V and under dark conditions. Top left inset: magnification of the high frequency region. Bottom right inset: equivalent circuit used for fitting the impedance of porous electrodes.

and transfer properties of the fibre samples over the nanoparticles. Thus, the charge transfer resistance at the TiO_2/electrolyte interface is 423, 137 and 259 Ω for TiO_2 Sol-gel, TiO_2 Fibres-A and TiO_2 Fibres B, respectively. First, a higher conductivity in the mesoporous fibres of interconnected nanoparticles is consistent with this kind of morphology [38]. Furthermore, electrospun samples present a lower charge transfer resistance than the TiO_2 Sol-gel sample, which could be attributed to the higher interface created since more oxygen vacancies and/or defects are formed during the fibres synthetic procedure, which can help in the charge transfer processes.

3.2. Catalytic performance in CO_2 photoreduction

The effect of morphological properties of hierarchical 1-D nanostructures and nanoparticles in the CO_2 photoreduction activity and selectivity using water as electron donor was investigated under UV light. Previous studies, performed in our group, in CO_2 photoreduction using TiO_2 anatase-type photocatalyst showed high selectivities towards the formation of syngas (CO and H_2) [10,39]. We show herein that the use of 1-D nanostructures leads to an increase in the CO_2 photoreduction mainly attributed to combination of enhanced charge separation and charge transfer processes.

Fig. 10 shows the kinetic profiles of the main products for all catalysts under UV irradiation in the CO_2 photoreduction reaction over 20 h. In all cases, these main products are CO, CH_4 and CH_3OH, along with H_2 coming from the concomitant H_2O reduction, plus lower amount of other C-containing products not shown in the figure. No products were found after performing blank reactions without any catalyst under dark and UV-vis illumination, nor in the presence of catalyst in dark conditions, discarding any CO_2 or H_2O conversion due to thermal or photochemical reactions or to thermal catalysis.

In general, the maximum production rates of CO and H_2 are reached after 6 h of irradiation. At longer reaction times, an increase in the production of CH_4 and CH_3OH is observed, which coincides with the decline in the production of CO and H_2, being the maximum production of these products close to 11 h of reaction time.

Table 2 shows the cumulative productions after 20 h reaction. The main products obtained with the TiO_2 Fibres A catalyst were H_2 and CO with lower amounts of CH_3OH and CH_4. The comparison of TiO_2 Fibres catalysts shows a better performance of the TiO_2 Fibres B catalyst, which presents an increase of nearly 3 times in the C-containing products and approximately 4 times in H-based obtained products. This is mainly due to a high CO and H_2 production with slightly higher production of CH_4. Interestingly, in the reaction with TiO_2 Fibres A, the amount of methanol produced is the highest in comparison with the rest of the catalysts. Nonetheless, the value of H-based obtained products is smaller than the value obtained with the other catalysts. Regarding the results obtained with TiO_2 Sol-gel, the selectivities with this catalyst and the TiO_2 Fibres B are similar, but in this case the amount of products is lower so that the values of converted H and converted C decrease. However, with the TiO_2 Fibres A catalyst a change in the selectivity is observed towards methane and methanol and lower productions of H_2, as seen in Fig. 11.

The changes in reactivity in the case of the TiO_2 fibres compared with nanoparticles can be mainly ascribed to the hierarchical nanostructure obtained for these catalysts during the electrospinning synthesis, which yields more closely packed grains improving the structural connections of TiO_2 crystals, thus favouring a fast charge transport along the grain boundaries, as it has been observed in the EIS studies. Moreover, the mixture of anatase and rutile phases observed in the TiO_2 Fibres B catalyst leads to a decrease in the photoluminescence intensity, indicating

Please cite this article in press as: P. Reñones, et al., Hierarchical TiO_2 nanofibres as photocatalyst for CO_2 reduction: Influence of morphology and phase composition on catalytic activity, J. CO_2 Util. (2016), http://dx.doi.org/10.1016/j.jcou.2016.04.002

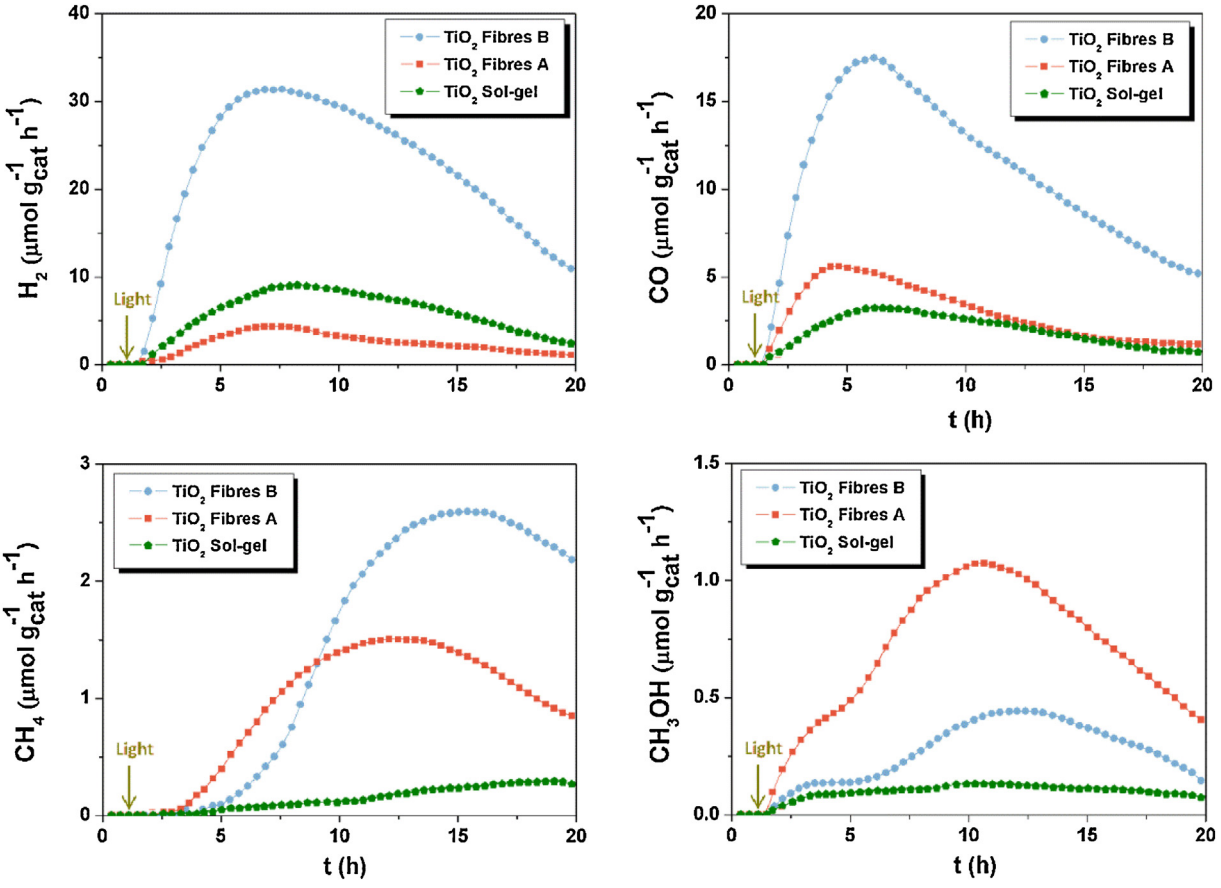

Fig. 10. Time evolution of products over TiO_2 Sol-gel, TiO_2 Fibres A and TiO_2 Fibres B catalysts in the CO_2 photoreduction reaction.

a reduction in the electron-hole recombination rate. This effect has been demonstrated to enhance the photocatalytic properties because of favoured electron transfer and transport processes [40]. Compared to commercial TiO_2 photocatalysts, the Fibres B sample shows a higher overall AQY (0.036%) than the usual benchmark P25 from Evonik (0.030%) tested in the same conditions, and higher than G5 from Millenium and PC500 from CrystalACTIV [10,39]. This further supports the interest of the samples studied in this work as CO_2 reduction photocatalysts. Regarding selectivity, the TiO_2 Fibres A catalyst shows, with respect to both Fibres B an Sol-gel, a higher tendency to form more electron demanding products as methanol and methane. EIS results have shown that the charge transfer resistance at the semiconductor-electrolyte interface is the lowest in this sample. This change in selectivity may be ascribed to a higher transfer rate of photogenerated carriers being beneficial to induce multi-electron reduction reactions.

4. Conclusions

Hierarchical assemblies of mesoporous TiO_2 1-D nanofibres have been successfully prepared by a combination of electrospinning and sol–gel methods and compared with TiO_2 nanoparticles obtained by a standard sol-gel procedure. The obtained fibres are composed of hierarchically arranged TiO_2 nanoparticles interconnected with large interfaces similar to grain boundaries, contrarily to the random aggregation found in TiO_2 Sol-gel sample. The phase composition (anatase:rutile ratio) of the fibre catalysts depend on the annealing conditions, with a static Ar atmosphere leading to a higher rutile amount than a dynamic one. Electrochemical impedance spectroscopy studies reveal a fast charge transport along the grain boundaries in fibre catalysts, which may be ascribed to an improved nanocrystals connection according to the materials physicochemical characterisation results. On the other hand, photoluminescence spectra show a decrease in the electron-hole recombination rate with higher rutile amount in the fibres samples. The combination of these features leads nanofibres to exhibit better results in CO_2 photoreduction than sol-gel photocatalyst. Among nanofibres, those containing a higher rutile amount (80:20) give rise to ca. 4 and 2.5 times higher H_2 and CO production, respectively, than those with 93:7 anatase: rutile ratio, in accordance with a lower electron-hole recombination rate. In turn, the latter gives rise to higher selectivities to

Table 2
Comparison of cumulative production ($\mu mol\, g_{cat}^{-1}$) in the CO_2 photoreduction reaction over the synthesised catalysts after 20 h of UV irradiation.

	H_2	CH_4	CO	C_{2+}	CH_3OH	*Converted C*[a]	*Converted H*[b]
TiO_2 Fibres A	42.78	18.16	55.06	3.36	15.14	98.9	250.1
TiO_2 Fibres B	398.84	26.88	203.91	6.89	5.04	253.4	977.7
TiO_2 Sol-gel	105.03	3.29	37.45	3.31	2.18	52.0	257.4

[a] Calculated as the sum of C atoms in C-containing products.
[b] Calculated as the sum of H atoms in H-containing products.

Please cite this article in press as: P. Reñones, et al., Hierarchical TiO_2 nanofibres as photocatalyst for CO_2 reduction: Influence of morphology and phase composition on catalytic activity, J. CO_2 Util. (2016), http://dx.doi.org/10.1016/j.jcou.2016.04.002

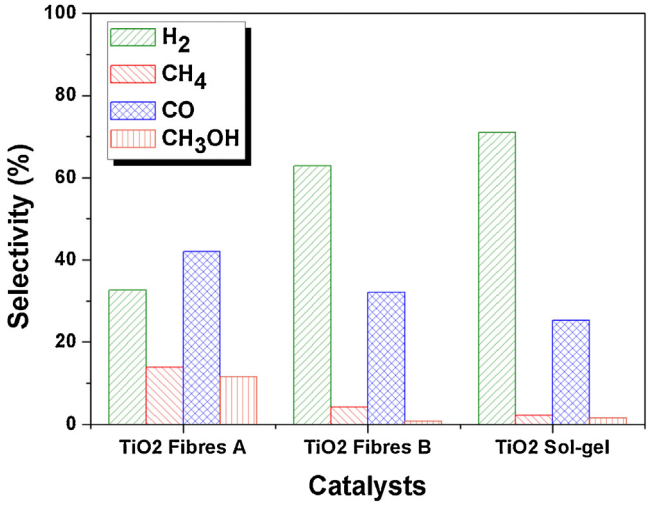

Fig. 11. Product selectivity over TiO_2 Fibres A, TiO_2 Fibres B and TiO_2 Sol-gel catalysts after 20 h of UV irradiation.

highly electron-demanding products such as methanol and methane, in line with a lower charge transfer resistance observed in EIS spectra.

Acknowledgements

This work, developed under the HyMAP project, has received funding from the European Research Council (ERC) under the European Union's Horizon 2020 research and innovation programme (grant agreement No. 648319). The results reflect only the authors' view and the Agency is not responsible for any use that may be made of the information they contain. Collaboration between groups has been developed under the MAD2D research program funded by *Comunidadde Madrid* (S2013/MIT-3007). F.F. thanks financial support from the European Union's Seventh Framework Programme (*AMAROUT-II PEOPLE-COFUND Action*, REA grant agreement No. 291803).

References

[1] A. de la Peña O'shea, D.P. Serrano, J.M. Coronado, From current challenges of CO_2 photocatalytic reduction over semiconductors using sunlight, in: E. Rozhkova, K. Ariga (Eds.), Molecules to Materials-Pathway to Artificial Photosynthesis, Springer, London, 2015.
[2] S. Protti, A. Albini, N. Serpone, Phys. Chem. Chem. Phys. 16 (2014) 19790.
[3] F. Fresno, R. Portela, S. Suárez, J.M. Coronado, J. Mater. Chem. A 2 (2014) 2863.
[4] X. Chen, S.S. Mao, Chem. Rev. 107 (2007) 2891.
[5] H. Xu, P. Reunchan, S.X. Ouyang, H. Tong, N. Umezawa, T. Kako, J.H. Ye, Chem. Mater. 25 (2013) 405.
[6] M. Mei, S. Chai, A. Rahman, Appl. Surf. Sci. 319 (2014) 37.
[7] J.H. Pan, H.Q. Dou, Z.G. Xiong, C. Xu, J.Z. Ma, X.S. Zhao, J. Mater. Chem. 20 (2010) 4512.
[8] J. Yu, H. Yu, B. Cheng, X. Zhao, Q. Zhang, J. Photochem. Photobiol. A Chem. 182 (2006) 121.
[9] T.A. Kandiel, R. Dillert, A. Feldhoff, D.W. Bahnemann, J. Phys. Chem. C 114 (2010) 4909.
[10] L. Collado, P. Jana, B. Sierra, J.M. Coronado, P. Pizarro, D.P. Serrano, V.A. de la Peña O'shea, Chem. Eng. J. 224 (2013) 128.
[11] M. Adachi, Y. Murata, J. Takao, J.T. Jiu, M. Sakamoto, F.M. Wang, J. Am. Chem. Soc. 126 (2004) 14943.
[12] J. Fan, L. Zhao, J. Yu, G. Liu, Nanoscale 4 (2012) 6597.
[13] Z.Y. Liu, D.D. Sun, P. Guo, J.O. Leckie, Nano Lett. 7 (2007) 1081.
[14] P.S. Archana, R. Jose, C. Vijila, S. Ramakrishna, J. Phys. Chem. C 113 (2009) 21538.
[15] H. Hou, L. Wang, F. Gao, G. Wei, J. Zheng, B. Tang, W. Yang, Int. J. Hydrogen Energy 39 (2014) 6837.
[16] H. Sun, B. Dong, G. Su, R. Gao, W. Liu, L. Song, L. Cao, Appl. Surf. Sci. 343 (2015) 181.
[17] A. Moya, A. Cherevan, S. Marchesan, P. Gebhardt, M. Prato, D. Eder, J.J. Vilatela, Appl. Catal. B: Environ. 179 (2015) 574.
[18] K.-I. Choi, S. Ho, J.-Y. Park, D.-Y. Choi, C.-H. Hwang, I.-H. Lee, M.H. Chang, Mater. Lett. 112 (2013) 113.
[19] N.A.M. Barakat, A.M. Hamza, S.S. Al-Deyab, A. Qurashi, H.Y. Kim, Mater. Sci. Eng. B. 177 (2012) 34.
[20] J. Zhang, S.-W. Choi, S.S. Kim, J. Solid State Chem. 184 (2011) 3008.
[21] A. Park, J. Moon, S.-J. Lee, S.H. Kim, T. Zyung, H.Y. Chu, Thin Solid Films 518 (2010) 6642.
[22] S. Madhugiri, B. Sun, P.G. Smirniotis, J.P. Ferraris, K.J. Balkus, Micropor. Mesopor. Mater. 69 (2004) 77.
[23] S.K. Choi, S. Kim, S.K. Lim, H. Park, J. Phys. Chem. C 114 (2010) 16475.
[24] S. Chuangchote, T. Sagawa, S. Yoshikawa, Appl. Phys. Lett. 93 (2008) 033310.
[25] A.L. Patterson, Phys. Rev. 56 (1939) 978.
[26] R.A. Spurr, H. Myers, Anal. Chem. 29 (1957) 760.
[27] D.A.H. Hanaor, C.C. Sorrell, J. Mater. Sci. 46 (2011) 855.
[28] M.M. Oliveira, D.C. Schnitzler, A.J.G. Zarbin, Chem. Mater. 15 (2003) 1903.
[29] M. Gotic, M. Ivanda, S. Popovic, S. Music, A. Sekulic, A. Turkovic, K. Furic, J. Raman Spectrosc. 28 (1997) 555.
[30] G.A. Tompsett, G.A. Bowmaker, R.P. Cooney, J.B. Metson, K.A. Rodgers, J.M. Seakins, J. Raman Spectrosc. 26 (1995) 57.
[31] K.-R. Zhu, M.-S. Zhang, Q. Chen, Z. Yin, Phys. Lett. 340 (2005) 220.
[32] D. Eder, A.H. Windle, J. Mater. Chem. 18 (2008) 2036.
[33] H. Yaghoubi, Z. Li, Y. Chen, H.T. Ngo, V.R. Bhethanabotla, B. Joseph, S. Ma, R. Schlaf, A. Takshi, ACS Catal. 5 (2015) 327.
[34] N. Serpone, D. Lawless, R. Khairutdinov, J. Phys. Chem. 99 (1995) 16646.
[35] O. Carp, C.L. Huisman, A. Reller, Prog. Solid State Chem. 32 (2004) 33.
[36] J. Liqiang, Q. Yichun, W. Baiqi, L. Shudan, J. Baojiang, Y. Libin, F. Wei, F. Honggang, S. Jiazhong, Sol. Energy Mater. Sol. Cells 90 (2006) 1773.
[37] F. Fabregat-Santiago, G. Garcia-Belmonte, J. Bisquert, A. Zaban, P. Salvador, J. Phys. Chem. B 106 (2002) 334.
[38] E. Ghadiri, N. Taghavinia, S.M. Zakeeruddin, M. Grätzel, J.-E. Moser, Nano Lett. 10 (2010) 1632.
[39] L. Collado, A. Reynal, J.M. Coronado, D.P. Serrano, J.R. Durrant, V.A. de la Peña O'Shea, Appl. Catal. B: Environ. 178 (2015) 177.
[40] D.O. Scanlon, C.W. Dunnill, J. Buckeridge, S.A. Sheylin, A.J. Logsdail, S.M. Woodley, C.R.A. Catlow, M.J. Powell, R.G. Palgrave, I.P. Parkin, G.W. Watson, T. W. Keal, P. Sherwood, A. Walsh, A.A. Sokol, Nat. Mater. 12 (2013) 798.

Please cite this article in press as: P. Reñones, et al., Hierarchical TiO_2 nanofibres as photocatalyst for CO_2 reduction: Influence of morphology and phase composition on catalytic activity, J. CO_2 Util. (2016), http://dx.doi.org/10.1016/j.jcou.2016.04.002